Optics Letters

In vivo broadband visible light optical coherence tomography probe enables inverse spectroscopic analysis

James A. Winkelmann,[1,*] Aya Eid,[1] The-Quyen Nguyen,[1] Thang Bui,[2] Ji Yi,[3,4] and Vadim Backman[1]

[1]Department of Biomedical Engineering, Northwestern University, 2145 Sheridan Rd., Evanston, Illinois 60208, USA
[2]Research Shop, Northwestern University, 2145 Sheridan Rd., Evanston, Illinois 60208, USA
[3]Department of Medicine, Boston University School of Medicine, 650 Albany St., Boston, Massachusetts 02118, USA
[4]Department of Biomedical Engineering, Boston University, 650 Albany St., Boston, Massachusetts 02118, USA
*Corresponding author: jameswinkelmann2014@u.northwestern.edu

Received 15 November 2017; accepted 19 December 2017; posted 5 January 2018 (Doc. ID 313344); published 1 February 2018

We report the design and characterization of a 6 mm outer diameter pull-back circumferential scanning visible optical coherence tomography probe. The probe's large visible bandwidth (500–695 nm) allowed for inverse spectroscopic analysis and an axial resolution of ∼1.1 μm in tissue. We verify spectral imaging capabilities by measuring microsphere backscattering spectra and demonstrate *in vivo* spatial nanoscale characterization of tissue.

OCIS codes: (110.4500) Optical coherence tomography; (300.0300) Spectroscopy; (170.3880) Medical and biological imaging.

https://doi.org/10.1364/OL.43.000619

Optical coherence tomography (OCT) is an optical imaging modality that acquires cross-sectional morphology of tissue by recording the coherent backscattered light off of a sample [1]. Traditionally used in ophthalmology, a new frontier of endoscope compatible OCT probes has resulted in the ability to image internal structures [2]. In addition to imaging, it has been demonstrated that by performing spectral analysis on the OCT signal, one can relate optical properties directly to tissue mass density distributions on length scales of 30–450 nm [3,4]. The technique to do this, known as inverse spectroscopic OCT (ISOCT), characterizes tissue's mass density auto-correlation function with a "shape factor" D. The autocorrelation function is a power law when D is between 0 and 3, stretched exponential between 3 and 4, exponential when equal to 4, and Gaussian as D approaches infinity [4]. The ultrastructure (sub-diffractional tissue morphology) sensitivity of D allows it to detect changes in collagen cross-linking and chromatin compaction, two morphological hallmarks of neoplasia, i.e., higher D infers more cross-linking and chromatin clumping. In fact, ISOCT has shown the ability to differentiate between healthy and pre-cancerous tissue that would otherwise appear histologically normal [4]. Hence, incorporating ISOCT analysis into endoscope measurements could provide physicians with a valuable risk stratification tool for various cancer types by providing a depth-resolved image of tissue ultrastructure.

Near-infrared (NIR) OCT probe technologies, such as micro-OCT and ultrahigh-resolution OCT, have pushed OCT resolution limits in endoscopy but ultrastructure sensitivity has yet to be demonstrated [5,6]. ISOCT relies on optical scattering to obtain D, so the higher the scattering, the higher the sensitivity of ISOCT. NIR is traditionally used in OCT probes because of tissue's low scattering coefficients in the NIR range, resulting in a high penetration depth. The visible spectrum's scattering coefficient is about double that of the NIR spectrum for tissue and as result has shallower penetration [7]. However, the higher scattering in the visible should increase OCT image contrast and ISOCT measurement sensitivity. The visible spectrum not only provides higher scattering contrast, but increases axial resolution and is sensitive to blood oxygenation [8,9]. Hence, a visible OCT endoscope is highly desirable for ultrastructural sensing, superior OCT imaging at superficial depths, and blood oxygenation measurements. Unfortunately, visible light is prone to severe focusing aberrations with traditional gradient index or ball lens OCT probe designs. A visible achromatic focusing OCT probe has been demonstrated previously, but it contained optics and scanning mechanisms not suitable for endoscope channel miniaturization [10]. Therefore, there is a need for a compact achromatic visible OCT probe that will allow for measurements *in vivo*.

Herein, we demonstrate, to the best of our knowledge, the first fiber-based pull-back circumferential scanning visible OCT probe with a 6 mm outer diameter. The probe has a bandwidth of 500–695 nm giving it the ability to spatially resolve tissue ultrastructure and perform high-resolution and contrast imaging. In fact, the probe has an axial resolution of 1.13 μm in tissue (tissue refractive index of $n = 1.33$), giving it superior imaging capabilities.

Assuming the sample is highly forward scattering, which is the case for most tissue, D can be quantified from the backscattering coefficient, $\mu_b(z, k)$, as shown in (1), where z is the axial depth location, and k is the wavenumber [4]:

$$\mu_b(z,k) \sim k^{4-D}. \quad (1)$$

The backscattering coefficient is computed through (2) using the short-time Fourier transform (STFT) OCT A-line intensity, $I(z,k)$, where $r(k)$ is the reference arm reflectance, L is the coherence length of the light source, $I_0(k)$ is the illumination intensity, and $\mu_s(k)$ is the scattering coefficient [4]:

$$\mu_b(z,k) = \frac{4\pi I^2(z,k)\exp(2z\mu_s(k))k^4}{r(k)I_0^2(k)L}. \quad (2)$$

The light source used was a supercontinuum (SuperK EXTREME, NKT Photonics) that was shaped using two prisms and a spatial filter to smooth out the power over different wavelengths and prevent saturation at the spectrometer. A broadband 50:50 fiber coupler (Thorlabs) then directed light towards the probe and reference arm mirror. A fiber polarization controller (Thorlabs) was placed in the reference arm fiber path to match polarization with the probe. Glass plates were placed in between the fiber output and reference arm mirror to match dispersion with the probe. Light collected from the probe and reference arm was interfered in the coupler and then directed towards a custom-built spectrometer. Light was delivered to the spectrometer from the coupler using a 50.8 mm focal length mirror collimator (Thorlabs). A 1300 lines/mm transmission grating (Wasatch) was used to angularly disperse the spectrum into a custom-built multi-element focusing objective (focal length = 123.7 mm) using off-the-shelf lenses (Edmund Optics) and 3D printed lens housing. A dual-line 4096 pixel camera (spL4096-140 km, Basler) was used to collect the light in the spectrometer in vertical binning mode. The spectrometer achieved a roll-off sensitivity of ~ − 15 dB/mm and an axial scan range of 1 mm. A picture and schematic of the probe is shown in Fig. 1. The probe utilized a 3.2 mm diameter distal motor (Precision Microdrives) to achieve circumferential scanning. Light was delivered to the probe using SM600 fiber (Thorlabs) that was stripped and inserted into a 1 mm diameter glass ferrule (AccuGlass). A 500 μm piece of 128 μm diameter coreless fiber (Thorlabs) was then fused onto the end SM600 fiber using a fusion splicer (Ericsson). This was done to prevent back reflections off the end of the fiber. The traditional epoxied angled spacer design could not be used due to epoxy absorption in the visible region, which resulted in burning of the epoxy. The ferrule was then inserted into a 2 mm outer diameter drive shaft. Light from the input fiber was collimated using an achromatic doublet (L1, focal length = 3 mm, Edmund Optics) and focused onto the sample using another achromatic doublet (L2, focal length = 12 mm, Edmund Optics), similar to a previously demonstrated NIR design [11]. Light was directed towards the sample with a 53° angled mirror attached to the distal motor. The angle was introduced to prevent back reflection off the outer glass sheath. The motor was aligned to the fiber and lenses using a piece of steel tubing with three viewing windows cut out. A custom piece of glass tubing (Technical Glass Products) encased the probe to shield it from biological fluids and serve as a stationary outer sheath. Pull-back scanning (maximum 1 cm) was accomplished by attaching the drive shaft to a motorized translational stage (Zaber Technologies). All data acquisition was accomplished using a custom-built interface with LabVIEW (National Instruments). Power at the sample was measured to be 8 mW. During all measurements

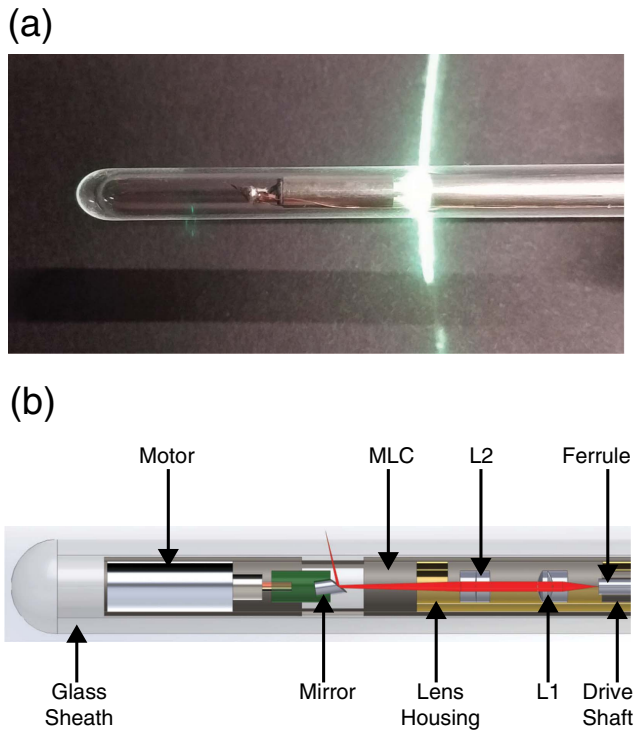

Fig. 1. (a) Photograph of ISOCT probe. (b) Schematic of ISOCT Probe; L1 (Lens 1, focal length = 3 mm); L2 (Lens 2, focal length = 12 mm); MLC (motor lens connector).

spectrometer acquisition parameters were set to collect 65,000 A-lines/sec at 15 μs exposure.

Ray-tracing software (Zemax Optics Studio 16) was used to estimate the probe's focusing performance according to the layout in Fig. 2(a). The analysis revealed a focus Gaussian waist size of 8.03 μm in the pull-back direction and 9.79 μm in the circumferential scanning direction with an astigmatic difference of 325 μm. The astigmatism, which can be visualized by the thru focus spot diagram in Fig. 2(b), is due to the outer glass sheath acting as a cylindrical lens [12]. The experimentally measured pull-back lateral resolution was found to be 9.64 μm by measuring the 50–50 transition distance edge-response of a razor blade placed at the focal point. Therefore, one can expect a similar degradation of ~2 μm in the circumferential direction from the measured 9.64 μm in accordance with the ray-trace

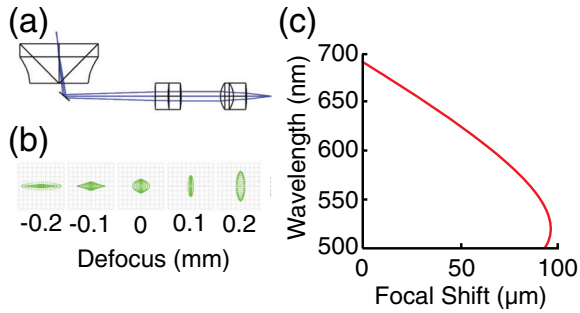

Fig. 2. Focusing aberration estimation. (a) Zemax layout. (b) Thru focus spot diagram for 600 nm. Grid Size = 2 × 2 μm. (c) Chromatic axial focal shift.

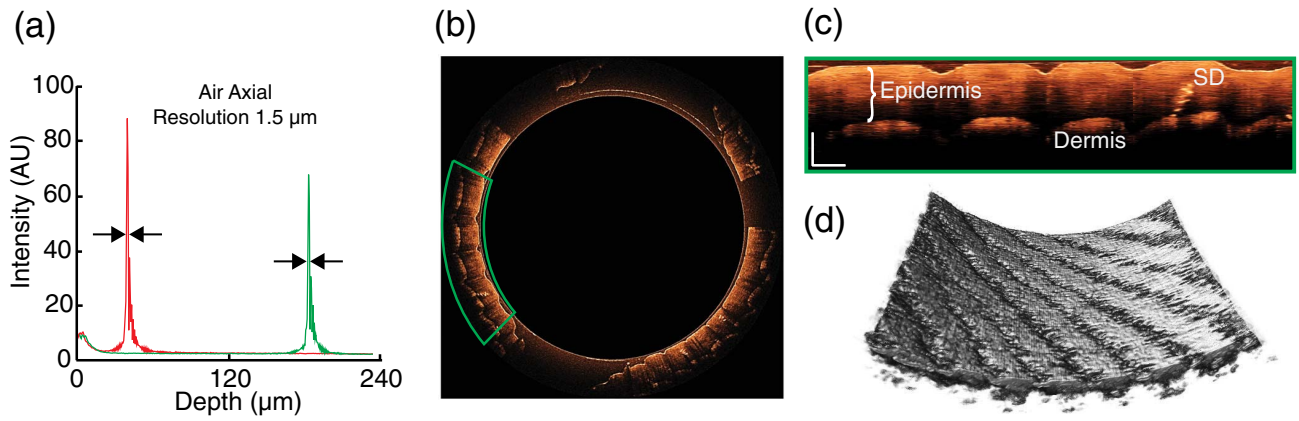

Fig. 3. Verifying probe imaging capabilities. (a) Mirror impulse response versus depth. Probe axial resolution was determined by measuring the full width at half max for each peak, which was found to be 1.5 μm in air for both. (b) OCT B-scan of the thumb and index finger pressed against the probe. (c) Zoom in B-Scan of green box in (b) showing anatomical structures; scale bar 250 μm. Sweat duct (SD). (d) 3D pull-back imaging of thumb; surface area = 4.6 × 3.2 mm.

simulation. Axial resolution was determined by measuring the impulse response function of a mirror at two different depths, as shown in Fig. 3(a). The full width at half max (FWHM) of the two peaks was found to be 1.5 μm, which corresponds to an axial resolution of ∼1.1 μm in tissue. To the best of our knowledge, this is the highest axial resolution OCT probe in publication.

Probe sample imaging was carried out in two modes: high resolution mode (motor speed: ∼20 rps, ∼3250 A-lines/B-scan, pull-back: 0.1 mm/s) and low resolution mode (motor speed: ∼40 rps, ∼1625 A-lines/B-scan, pull-back: 0.5 mm/s). All three-dimensional pull-back images contained in this Letter were acquired in low-resolution mode, while B-scans were obtained in high-resolution mode. To demonstrate the probe's imaging capabilities, a thumb and finger were scanned, as shown in Figs. 3(b)–3(d). It can be seen in Fig. 3(b) that the probe achieved imaging throughout the circumference. In Fig. 3(c), the effect of having ∼1.1 μm axial resolution can be visualized with crisp surfaces and well-defined anatomical features, such as epidermal thickness and a sweat duct. Figure 3(d) shows the pull-back capabilities allowing one to visualize large fields of view for three-dimensional imaging.

After verifying the probe's imaging abilities, spectroscopic imaging performance was characterized. While the achromatic doublet design minimized chromatic aberrations, the ray trace showed a chromatic focal shift of 96.1 μm still existed in the spectrum, as shown in Fig. 2(c). Furthermore, the axial point spread function was not uniform along the circumferential scan due to the beam being slightly off axis from the center of the probe, creating different focal points at different scanning angles, θ. In order to calculate μ_b, the OCT A-line intensity, $I(z, k, \theta)$, as a function of depth, wavenumber, and angle needed to be determined to normalize measurements. This was accomplished by measuring a calibration 60 nm bead aqueous solution. The solution was prepared by diluting 60 nm latex microspheres (Thermo Scientific) to 1% concentration with deionized water. This resulted in a reduced scattering coefficient of 5.87 cm^{-1} at 500 nm for the aqueous calibration standard, which is similar to that of tissue [7]. Three latex microsphere sizes (100 nm, 370 nm, and 650 nm, Thermo Scientific) were then measured in high-resolution mode and compared with Mie theory to verify the probe's spectroscopic performance. All aqueous latex microsphere solutions were diluted to a concentration of 1% with deionized water. Backscattering coefficients were calculated by computing the STFT of each B-scan using 26 constant wavenumber width Gaussian windows with a FWHM of 15 nm for the center wavelength. This increased ISOCT measurement axial voxel size to ∼13 μm. $I(z, k, \theta)$ of the sample was divided by its respective calibration $I(z, k, \theta)$ from the 60 nm calibration solution, squared and then multiplied by k^4 to obtain the back scattering spectra shape. Back scattering spectra were averaged from the surface to 160 μm into the bead solution for 152 B-scans in high-resolution scan mode. The surface was found using an in-house surface detection algorithm. As shown in Fig. 4 the measured mean normalized backscattering coefficients had good agreement with theory, illustrating the probes' ability to perform spatial spectral analysis. Furthermore, the D values quantified from the 100 nm Mie theory spectra and

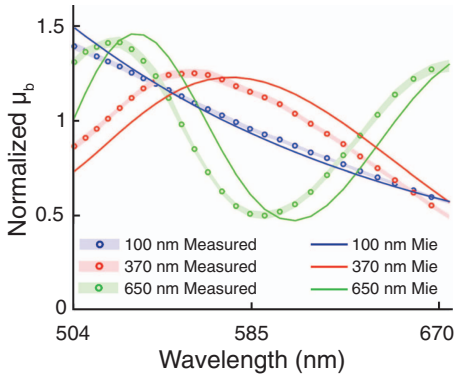

Fig. 4. Mean normalized backscattering spectra of latex microsphere solutions diluted with deionized water. Bead diameters: 100 nm (≤ 15%CV), 370 nm (≤ 3%CV), 650 nm (≤ 3%CV). Measured values are an average of 152 B-scans from bead surface to 160 μm into solution. Shaded region is standard error between B-scans. Coefficient of variation (CV) = diameter standard deviation over the mean.

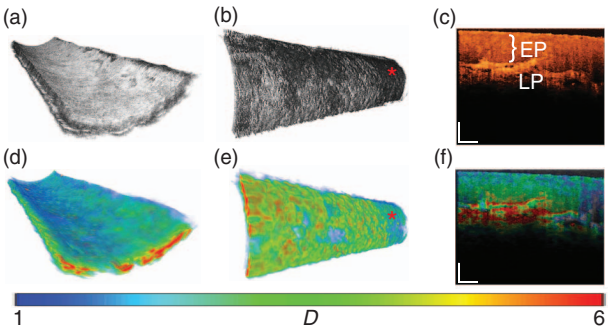

Fig. 5. *In vivo* imaging of bottom lower lip with structural image top row and corresponding D map bottom row; (a) and (d) above and (b) and (e) bottom perspective of 3D pull-back. Red asterisk indicates portion of the scan with thicker epithelium layer, resulting in LP not being visible and lower D values. (c) B-Scan showing anatomical features; epidermis (EP), lamina propria (LP). (f) B-Scan with D map overlay. (a), (b), (d), and (e) Surface area = 4.7 × 10 mm. (c) and (f) Scale bars $H = 150$ μm, $W = 450$ μm.

measured spectra suggest a D measurement accuracy of 0.3 for the probe.

To demonstrate *in vivo* spectral analysis, the bottom inner lip was imaged from a healthy volunteer. Structural (top row) and corresponding ultrastructural D pseudocolor map (bottom row) images can be seen in Fig. 5. Normalized $\mu_b(z, k, \theta)$ for lip tissue was calculated in the same manner as microsphere solutions. D was then calculated by fitting a power law as a function of k to $\mu_b(z, k, \theta)$ and convolving with a spatial averaging window with a size of 140 × 21 × 75 μm (B-Scan X axial X pull-back). The epithelium and lamina propria (LP) can clearly be seen in the structural images. The ultrastructural analysis revealed higher D values for the LP ($D = 5.22 + -0.09$) compared to the epithelium ($D = 3.26 + -0.02$). Epithelium thickness varied significantly across the 3D scan, resulting in the LP being too deep for imaging as shown by the darker intensities (red asterisk) in Fig. 5(b). Epithelium thickness is also evident in Fig. 5(e) with smaller D values (red asterisk) being correlated with the thicker epithelium parts of the scan. Likewise, in Fig. 5(f), the transition from epithelium to LP is marked by an increase in D values.

The D value difference among anatomical layers is indicative of the different nanoscale organizations of these tissue layers. The extracellular matrix, which is abundant in the LP, has been reported to have a higher D compared to that of epithelial tissues when measured with ISOCT due to a difference in nanoscale heterogeneity [3]. Previous studies have demonstrated that D increases in early carcinogenesis in both the epithelium (in part due to chromatin alterations in cell nuclei) and the extracellular matrix (in part due to collagen matrix cross linking) [4]. These alterations occur at length scales typically not discernable on microscopic images. This underlies the need to measure D *in vivo*. We have demonstrated that visible OCT endoscopy provides this capability. A weakness of the approach reported here is that tissue D values in Fig. 5 might contain errors due to the inability to mask out blood vessels in the ultrastructural analysis. Therefore, microangiography capabilities are highly desired for future applications to allow for separate spectral analysis on the pericapillary space and blood vessel network.

In summary, we have developed the first fiber-based pull-back circumferential scanning visible OCT probe. We demonstrated the probe's morphological imaging capabilities and ability to perform spectroscopic analysis. Future plans will aim to reduce the diameter to 2 mm by utilizing 1 mm diameter lenses (Edmund Optics) and motor (Kinetron). This will facilitate microangiography and endoscope compatibility.

Funding. National Science Foundation (NSF) (EFRI-1240416); National Institutes of Health (NIH) (R01CA165309, R01CA183101).

REFERENCES

1. D. Huang, E. A. Swanson, C. P. Lin, J. S. Schuman, W. G. Stinson, W. Chang, M. R. Hee, T. Flotte, K. Gregory, C. A. Puliafito, and J. G. Fujimoto, Science **254**, 1178 (1991).
2. T.-H. Tsai, O. O. Ahsen, H.-C. Lee, K. Liang, M. G. Giacomelli, B. M. Potsaid, Y. K. Tao, V. Jayaraman, M. F. Kraus, J. Hornegger, M. Figueiredo, Q. Huang, H. Mashimo, A. E. Cable, and J. G. Fujimoto, Proc. SPIE **8927**, 89270T (2014).
3. J. Yi, A. J. Radosevich, J. D. Rogers, S. C. P. Norris, I. R. Çapoğlu, A. Taflove, and V. Backman, Opt. Express **21**, 9043 (2013).
4. J. Yi, A. J. Radosevich, Y. Stypula-Cyrus, N. N. Mutyal, S. M. Azarin, E. Horcher, M. J. Goldberg, L. K. Bianchi, S. Bajaj, H. K. Roy, and V. Backman, J. Biomed. Opt. **19**, 36013 (2014).
5. D. Cui, K. K. Chu, B. Yin, T. N. Ford, C. Hyun, H. L. Min, J. A. Gardecki, G. M. Solomon, S. E. Birket, L. Liu, S. M. Rowe, and G. J. Tearney, Opt. Lett. **42**, 867 (2017).
6. J. Xi, A. Zhang, Z. Liu, W. Liang, L. Y. Lin, S. Yu, and X. Li, Opt. Lett. **39**, 2016 (2014).
7. S. L. Jacques, Phys. Med. Biol. **58**, R37 (2013).
8. S. Chen, X. Shu, J. Yi, A. Fawzi, and H. F. Zhang, J. Biomed. Opt. **21**, 66013 (2016).
9. J. Yi, S. Chen, V. Backman, and H. F. Zhang, Biomed. Opt. Express **5**, 3603 (2014).
10. L. Duan, M. D. Mcraven, R. S. Veazey, T. J. Hope, H. F. Zhang, L. Duan, M. D. Mcraven, W. Liu, X. Shu, J. Hu, C. Sun, R. S. Veazey, T. J. Hope, H. F. Zhang, L. Duan, M. D. Mcraven, W. Liu, X. Shu, J. Hu, C. Sun, and R. S. Veazey, J. Biomed. Opt. **22**, 056003 (2017).
11. A. R. Tumlinson, B. Považay, L. P. Hariri, J. McNally, A. Unterhuber, B. Hermann, H. Sattmann, W. Drexler, and J. K. Barton, J. Biomed. Opt. **11**, 64003 (2006).
12. J. Xi, L. Huo, Y. Wu, M. J. Cobb, J. H. Hwang, and X. Li, Opt. Lett. **34**, 1943 (2009).